Optics Letters

Dispersion diagram of surface plasmon polaritons from angular transmission investigation

Gian Paolo Papari,[1,2,3,*] Zahra Mazaheri,[1] Can Koral,[3] and Antonello Andreone[1,2,3]

[1]Dipartimento di Fisica, Università di Napoli "Federico II," via Cinthia, I-80126 Napoli, Italy
[2]CNR-SPIN, UOS Napoli, via Cinthia, I-80126 Napoli, Italy
[3]Istituto Nazionale di Fisica Nucleare (INFN), Naples Unit, via Cinthia, I-80126 Napoli, Italy
*Corresponding author: gianpaolo.papari@unina.it

Received 18 February 2021; accepted 12 April 2021; posted 21 April 2021 (Doc. ID 423048); published 18 May 2021

A novel, to the best of our knowledge, methodology based on the combination of experimental measurements and simulations of the wave transmission through a metasurface at different angles is presented, enabling us to identify the fundamental and first high-order mode of spoof surface plasmon polaritons (SSPPs) excited in the terahertz regime. The approach offers a new way, an alternative to standard near field imaging, to trace out the presence of SSPPs on a metal-dielectric interface.

https://doi.org/10.1364/OL.423048

Surface plasmon polaritons (SPPs) are electromagnetic (EM) waves propagating at the boundary between a metal and an insulator [1,2]. The possibility to couple an external EM wave within a metal-dielectric interface, along with the peculiar mode properties, has attracted enormous interest for decades. Indeed, SPPs represent on one side a valuable strategy towards electronics/photonics integration in all-optical circuits (for example, to realize a fast, wireless input/output communication channel with electronic devices [3,4]); on the other hand, they can be exploited for label free-sensing [5,6], the generation of orbital angular momentum [7], and sub-wavelength imaging [8]. SPPs refer to surface collective excitations of the electronic fluid [1], activated when the frequency of the light interacting with the mobile conduction charges is of the order of the metal plasma frequency ω_p at the interface [1]. ω_p in ordinary metals can be as high as 10^{15} Hz [9]; however, the introduction of "dilute metals," obtained for example by the removal of conducting patches to realize a simple metagrid [10], can lower the effective plasma frequency for SPPs ω_r down to the terahertz or even gigahertz band [11]. In these structured surfaces, spoof SPPs (SSPPs) created by design are characterized by a dispersion diagram [12] perfectly equivalent to the SPP case. Therefore, in the following, we will discuss SSPPs as a particular case of the more general SPP dispersion diagram.

In Fig. 1, the expected dispersion relation for the SSPP fundamental mode (FM) [12] and first high-order mode (HOM) is reported [13,14]. The FM first follows the light line at low frequencies; then it asymptotically approaches ω_r at large wavevector k values. The peculiar characteristic of the FM to lie below the light line is a signature of a bound state at a metal-dielectric interface. Above ω_r, HOMs show a leaky/radiative behavior, since they can couple with the continuum [1]. In metagrids, they are responsible for the light "tunneling" through the metasurface [2]. SPP excitations on a metal-dielectric interface can be visualized through near field measurements [15–17]. The relative dispersion relation can be computed using full wave numerical methods [15,18]. In the standard experimental approach, $\omega(k)$ diagrams of metagrids are usually obtained via angular measurements through the analysis of the modulus of the complex transmission $\tilde{T}$.

This type of investigation, however, enables us to describe HOMs only [13,19,20]. Actually, the FM is hard to detect since, for $\omega < \omega_r$, the metagrid behaves as a homogeneous metallic mirror [14], and the transmitted signal is extremely low. Indeed, the possibility to directly observe the FM represents relevant information for predicting the presence of SPP excitations [12] on a metasurface.

The aim of this Letter is to present a method based on transmission experiments and full wave simulations in order to extract the dispersion diagram of both the FM and first HOM. The experimental results are compared with a computed dispersion diagram (CDD) obtained using an eigenmode solver. The proposed approach enables us to visualize the fingerprint of SPPs in the $\omega(k)$ spectrum and address their onset, providing a further way to monitor their existence besides the

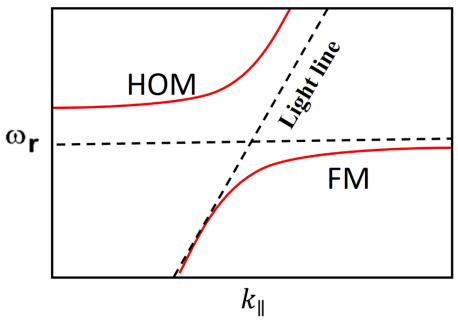

Fig. 1. Dispersion diagram for the spoof SPP FM and first HOM on a structured conducting surface. The light line $\omega = ck$ and the asymptotic SPP effective plasma frequency ω_r are shown as dashed lines.

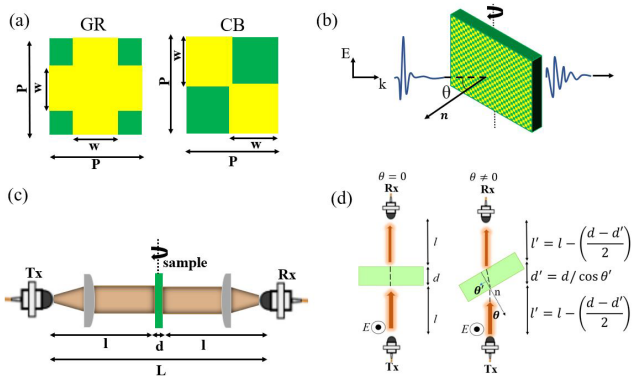

Fig. 2. (a) Sketch of the unit cells of the different metasurfaces under study (GR, grid; CB, chessboard). (b) Details of the terahertz beam (TE polarization) impinging on the sample plane at the incidence angle θ. (c) Pictorial representation of the setup, with indication of the optical paths. (d) Sketch of the Tx-Rx optical path covered during the experiment versus the incidence angle.

well-established imaging technique. We experimentally investigate the dispersion diagram of two different "dilute metals" in the shape of conducting grids, measuring $\tilde{T}$ as a function of the angle between the incident radiation and each metasurface [Fig. 2(a)].

Analogous to other reports [21,22], in order to retrieve the $\omega(k)$ relation for the metasurface eigenmodes, one can study the dependence of maxima and minima on frequency f and impinging angle θ in the modulus contour plot $|\tilde{T}(f,\theta)|$. However, using a standard approach, low frequency modes in $|\tilde{T}(f,\theta)|$ can be only partially visualized or are not visible at all, making difficult a meaningful comparison with results extracted through the CDD. To circumvent this problem, we propose a different set of observables containing more information than $|\tilde{T}(f,\theta)|$. Specifically, our insight consists of using the real part of the normalized electric field, $E_N(f,\theta) = |\tilde{T}(f,\theta)|\cos\phi_s$, where the cosine argument ϕ_s represents the accumulated phase of the signal passing through the sample. As explained in detail below, ϕ_s contains a great wealth of information, allowing us to unambiguously unveil the presence in the dispersion diagram of eigenmodes, even if only weakly coupled with the metasurface.

Experimentally, angular measurements face a tough difficulty into acquiring the transmitted signal, since as θ increases more and more signal is reflected, reducing the signal-to-noise ratio. Wave transmission is particularly degraded for $f < \omega_r/2\pi$, mostly affecting the phase of the signal. To overcome this problem, we have developed a computational strategy to extract the dispersion diagram directly from the Fourier transform of the electric fields. Once $E_N(f,\theta)$ is acquired, the $\omega(k)$ spectrum is clearly determined by the local stationarity of both minima and maxima in its contour plot.

Time domain spectroscopy in the terahertz band has been applied to measure the transmission properties of two different metagrids in the nearness of the plasma frequency. Both metasurfaces have been fabricated through chemical and galvanic processes and are sketched in Fig. 2(a), where the relevant geometrical lengths are reported. 30 μm thick copper is deposited on a standard FR4 substrate (thickness 160 μm). The two samples belong to the family of fishnet metasurfaces, with the metallic layer patterned as a grid (GR) and a chessboard (CB), respectively, and presenting same stripe width $w = 300$ μm and periodicity $P = 600$ μm.

In a previous paper [18], we have shown, both analytically and experimentally, that these dilute metallic structures display a different and peculiar electromagnetic behavior. A detailed study on the dependence of the effective plasma frequency ω_r for high-order SPPs on the metal filling factor F (which in turn depends on the unit cell size) was reported.

Measurements are carried out using a commercial spectrometer (TERA K15 from Menlo Systems) based on photo-antenna technology for both wave generation and detection. Pulsed signals are acquired for a time interval $\Delta t = 200$ ps, which corresponds to a spectral resolution Δf of about 3 GHz. To reduce the effect of water absorption in the terahertz signal, the time-dependent electric field is recorded keeping the optical setup in a dry box purged with nitrogen gas (humidity level below 0.1%). Transmission measurements and relative simulations were performed in TE and TM polarization by setting the electric field, respectively, parallel and perpendicular to the rotation axis of the sample. As pictorially described in Fig. 2(b) (TE polarization), the collimated beam is directed towards the surface oriented according to a specific angle starting from 0°. To avoid diffraction effects produced by the interaction between the beam and the sample holder, the angular range is upwardly limited to 50°. In Fig. 2(c), the sketch of the experiment is reported. The distance between the transmitter (Tx) and the receiver (Rx) is kept constant and, in the absence of a sample, can be expressed as $L = 2l + d$, where l is the free-space optical path to and from the metasurface and d is the sample thickness.

In Fig. 2(c), the sketch of the experiment is reported. The distance between the transmitter (Tx) and the receiver (Rx) is kept constant and can be expressed as $L = 2l + d$, where l is the free-space optical path to and from the metasurface, and d is the sample thickness. The sample is free to rotate along an axis parallel to the impinging electric field. Obviously, under this configuration, the overall distance Tx-Rx does not depend on θ, whereas the optical path does. In fact, as shown in Fig. 2(d), as the sample is rotated, the travel distance inside the sample (having $\tilde{n} = n + ik$ as complex refractive index) increases up to $d' = d/\cos\theta'$ ($\theta' = \arcsin(1/n)$), whereas the free-space path decreases down to $l' = l - (d' - d)/2$.

In order to study the dependence $\omega\, vs\, k_\parallel$ in the dispersion diagram ($k_\parallel$ being the component of the wavevector parallel to the plane), the plot $E_N(f,\theta)$ is acquired. This is done recording the time-dependent electric field $E_{r,s}(t)$ of the signal transmitted through free space (reference r field) and through the metasurface (sample s field). Using fast Fourier transform, one can evaluate both $|\tilde{E}_r(f)|$ and $\tilde{E}_s(f,\theta) = |\tilde{E}_s(f,\theta)|\exp\{i\phi_s(f,\theta)\}$, where $\phi_s(f,\theta)$ is the phase collected during the travel between transmitter and detector antennas when the sample is placed between. The real part of the normalized electric field is then simply obtained considering the cosine of the phase in the presence of the sample: $E_N = |\tilde{E}_s|/|\tilde{E}_r|\cos\phi_s = |\tilde{T}|\cos\phi_s$. The numerical analysis of the metasurface response is performed by employing the commercial software CST Microwave Studio. In particular, for the simulation of $\tilde{E}_N(f,\theta)$, we use a frequency domain solver within a "unit cell" size varying the impinging angle between 0° and 70°.

A CDD is calculated by means of an eigenmode solver, where the unit cell of the periodic surface is kept between two perfect electric boundaries (held at the same distance of the

transmission/detection ports used in the frequency mode). We show here that the complex electric field transmitted through a metasurface can be simply expressed using its own eigenmodes. Since $k_\parallel$ is directly proportional to θ, and given $\omega = 2\pi f$, in the following, we will indicate the dispersion diagram of the mth eigenmode as $f_m(\theta)$ in place of $\omega_m(k_\parallel)$.

The electric field of the reference signal received by the detector, after the path L, can be written as

$$\tilde{E}_r(f) = \left|\tilde{E}_r(f)\right| e^{i\phi_r} = \left|\tilde{E}_r(f)\right| e^{-\frac{i2\pi fL}{c}}, \tag{1}$$

where c is the speed of light in vacuum.

Analogously, the electric field transmitted through the metasurface can be written as

$$\tilde{E}_s(f,\theta) = \left|\tilde{E}_s(f,\theta)\right| e^{-i\phi_s}, \tag{2}$$

where $\phi_s(f,\theta) = \frac{2\pi f}{c}[2l'(\theta) + n(f)d'(\theta)]$, and $n(f)$ is the real part of the refractive index of the metasurface.

$\tilde{E}_s$ also can be made explicit in terms of the first M eigenmodes of the metasurface:

$$\tilde{E}_s(f,\theta) = \left|\tilde{E}_s(f,\theta)\right| e^{i2l'\frac{2\pi f}{c}} e^{in(f)d'\frac{2\pi f}{c}} = \sum_{m=1}^{M} \tilde{A}_m(f,\theta)\, E_m[f_m(\theta)]\, e^{i\frac{2\pi f}{c}\{n_m[f_m(\theta)]d' + 2l'\}}. \tag{3}$$

In Eq. (3), the electric field is decomposed in the base of eigenmodes, characterized by their own delay and absorption described by n_m. Each term in the sum therefore depends on n_m and on the incidence angle through the dispersion curve $f_m(\theta)$. The complex coefficient $\tilde{A}_m(\omega,\theta)$ expresses the relative weight of the mth eigenmode.

Since we are interested in the real part of $\tilde{E}_s$ we set

$$\tilde{A}_m(f,\theta) = \left|\tilde{A}_m(f,\theta)\right| e^{i\alpha(f,\theta)}, \tag{4}$$

and the electric field in Eq. (3) becomes

$$\tilde{E}_s(f,\theta) = \sum_{m=1}^{M} A_m(f,\theta)\, E_m[f_m(\theta)]\, e^{i\frac{2\pi f}{c}\{n_m[f_m(\theta)]d' + 2l'\} + i\alpha(f,\theta)}. \tag{5}$$

Under these assumptions, the normalized electric field parameter can be written as

$$\tilde{E}_N(f,\theta) = \sum_{m=1}^{M} a_m(f,\theta)\, E_m[f_m(\theta)]\, e^{i\frac{2\pi f}{c}\{n_m[f_m(\theta)]d' + 2l'\} + i\alpha(f,\theta)}, \tag{6}$$

where $a_m(f,\theta) = A_m(f,\theta)/E_r(f,\theta)$.

Therefore, Eq. (6) in its general formulation shows that both the modulus and phase of $\tilde{E}_N$ contain information on the dispersion diagram of a metasurface. Consequently, the real part E_N turns out to be a valuable function to retrieve the dispersion curve for eigenmodes, which are characterized by resonances which in turn reflect the enhanced coupling of the radiation with the metasurface. The function E_N displays a more pronounced dynamics of eigenmodes, in comparison with the simple modulus because, in correspondence with an eigenmode, $n(\theta,\omega_m)$ [23] peaks (in terms of maximal or minimal value), and $\alpha = 0$.

Moreover, we will show that a direct experimental observation of the overlapping between CDD eigenmodes and maxima/minima in $E_N(f,\theta)$ fosters the search for stationary points f_m in the function E_N, which is

$$dE_N(f,\theta)_{f=f_m} = 0. \tag{7}$$

Fulfillment of Eq. (7) implies that, in correspondence with a specific eigenmode identified by the pair of independent parameters (f_m,θ), the system of equations

$$\begin{cases} \frac{dE_N}{df} = 0 \\ \frac{dE_N}{d\theta} = 0 \end{cases}, \tag{8}$$

must be verified.

Since

$$dE_N(f,\theta) = (dE_N/df)\, df + (dE_N/d\theta)\, d\theta, \tag{9}$$

the condition in Eq. (7) suggests defining a function $df/d\theta$ that is regular only along the eigenmode dispersion:

$$K(f,\theta) = df/d\theta = -\frac{dE_N}{d\theta}\left(\frac{dE_N}{df}\right)^{-1} \quad \text{for } f \to f_m. \tag{10}$$

Actually, the kernel of the differential operator dE_N is the collection of 0/0 singular points [Eq. (8)] whose convergence might occur only in the presence of a continuous function of parameters f and θ. Instead, the discrete nature of the function E_N-realized with different sampling of the two independent parameters (f,θ)–implies that from the whole K contour plot the eigenmode dispersion is defined by a close (but not overlapping) couple of points, the first one extremely small (since it depends on $dE_N/d\theta$) and the other one (proportional to $(dE_N/df)^{-1}$) extremely large. The behavior of the $K(f_m,\theta)$ function enables us to distinctly trace out both the FM and the first HOM through their respective contour plots.

In order to validate the simulated results, we show in Fig. 3 the comparison between the simulated and experimental modulus $|\tilde{E}_N|$ of the metagrid (GR) in the range $(f,\theta) \equiv [(0.1 - 0.7)\,\text{THz}, 0° - 50°]$. The reliability of the experimental results is well proven by corresponding simulations, although the experimental phase ϕ_s of $\tilde{E}_N$ suffers from a low signal-to-noise ratio that decreases as θ increases. Therefore, to recover the phase dynamics in the following we rely on a simulation only. Since we are interested in tracing out the dispersion relation for the lowest energy modes, we select the frequency range (0.10–0.24 THz) corresponding to the first two eigenmodes (the fundamental and the first HOM). In order to highlight the significance of E_N to show the eigenmode

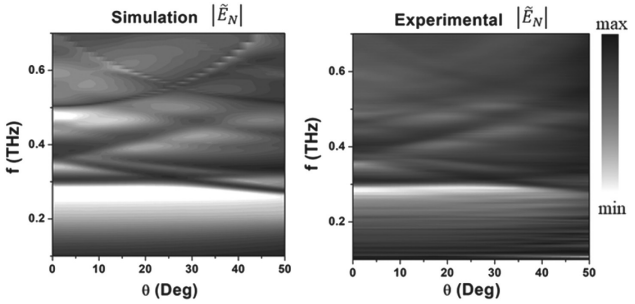

Fig. 3. Comparison between the simulated and the experimental $|\tilde{E}_N(f,\theta)|$ plot for the GR metasurface.

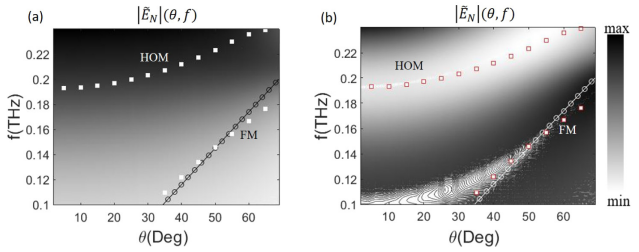

Fig. 4. Contour plot of the (a) modulus and (b) real part of $\tilde{E}_N$ for the GR metasurface. The FM and first HOM are reported in both plots. The black and white circles in the figures represent the light line.

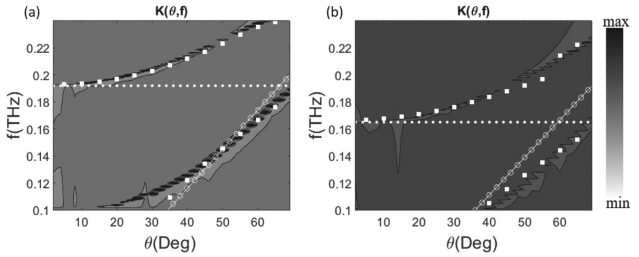

Fig. 5. Contour plot of the function $K(f,\theta)$ [see Eq. (8)] for the (a) GR and (b) CB metasurface. The white circle curve represents the light line, and the white dotted line shows the metasurface plasma frequency.

dispersion diagram, we report the comparison between $|\tilde{E}_N|$ [Fig. 4(a)] and E_N [Fig. 4(b)] with the outcomes of the CDD. Both figures clearly show that the latter quantity, being a function of the accumulated phase ϕ_s, provides more information on the minima and maxima dynamics, which better identifies the FM and the first HOM behavior.

In the end, we report in Figs. 5(a) and 5(b) the function $K(f,\theta)$ for the GR and CB metasurface, respectively. The series of singular points highlights the curves $K(f_m,\theta)$ referred to as both the FM and the first HOM. The curves are in reasonable agreement with the expected eigenmode dispersion depicted in Fig. 1. Through this procedure, the FM is completely traced out, revealing the activation and propagation of SSPPs along the metal-dielectric interface.

However, from the plot, one can observe that the FM for the GR metasurface does not follow the expected trend, tangential to the light line at small angles. Different from the ideal case, the FM crosses the light line at a given angle. The origin of this mismatch comes from the averaging effect produced by the electric field at large wavelengths, which couples with an effective interface consisting of a dilute (Drude-like) metal layer and a weak metallic, rather than a dielectric layer. It can be shown in fact that for large impinging wavelengths, comparable with the metasurface thickness, the resulting dispersion function for the FM can be modeled through the SPP dispersion relation $k_{\parallel}=\frac{\omega}{c}\sqrt{\frac{\varepsilon_d\varepsilon_m}{\varepsilon_d+\varepsilon_m}}$, provided that ε_d has a weak metallic behavior ($\varepsilon_d \leq 0$), and ε_m can be modeled with a Drude function, depending on the effective plasma frequency ω_r. The crossing angle ($\sim 50°$) represents the threshold at which the impinging radiation can effectively activate the SPP propagation, since the metasurface properly behaves as a metal-dielectric interface.

It is worthwhile to observe that the CB geometry shows an effective plasma frequency $\omega_{r,\mathrm{CB}}/2\pi$ smaller than the GR geometry because of the different amounts of metal filling the unit cell [20]. Therefore, the former metasurface displays a FM dispersion departing from the light line at smaller angles with respect to the latter one [see Fig. 5(b)]. This evidence suggests better use, at a fixed periodicity and patch size, of the CB design as a unit cell to exploit propagation of SPP waves at its finest.

In conclusion, we have presented a method to trace out the FM and the first HOM of a metasurface by employing the normalized electric field E_N. We show that investigation of eigenmode dispersion is better reproduced by employing the real part of $\tilde{E}_N$ in place of its modulus. This approach provides a clear signature of SPP activation, even if the electromagnetic coupling providing the onset of spoof SPPs is weak. The combination of experimental data with appropriate simulations paves the way to the discernment of the onset and propagation of SPPs, becoming a precious guide to detect the minimal angle for the activation of the SPP along the metasurface. The activation angle is achieved in correspondence with the separation between the FM and the light line.

Funding. Instituto Nazionale di Fisica Nucleare.

Acknowledgment. This work was conducted under the aegis of INFN (Instituto Nazionale di Fisica Nucleare) and supported by the project TERA.

Disclosures. The authors declare no conflicts of interest.

Data Availability. Data underlying the results presented in this paper are not publicly available at this time but may be obtained from the authors upon reasonable request.

REFERENCES

1. R. H. Ritchie, Surf. Sci. **34**, 1 (1973).
2. F. J. Garcia-Vidal, L. Martin-Moreno, T. W. Ebbesen, and L. Kuipers, Rev. Mod. Phys. **82**, 729 (2010).
3. E. Ozbay, Science **311**, 189 (2006).
4. K. F. MacDonald, Z. L. Sámson, M. I. Stockman, and N. I. Zheludev, Nat. Photonics **3**, 55 (2009).
5. Z. Dong, H. Liu, J. Cao, T. Li, S. Wang, Z. Dong, H. Liu, J. Cao, T. Li, S. Wang, and S. Zhu, Appl. Phys. Lett. **97**, 114101 (2010).
6. G. P. Papari, C. Koral, and A. Andreone, Sensors **19**, 2544 (2019).
7. Y. Yuan, K. Zhang, B. Ratni, Q. Song, X. Ding, Q. Wu, S. N. Burokur, and P. Genevet, Nat. Commun. **11**, 4186 (2020).
8. X. Luo and L. Yan, IEEE Photonics J. **4**, 590 (2012).
9. C. Kittel, *Introduction to Solid State Physics* (Wiley, 1953).
10. G. P. Papari, J. J. J. Nivas, C. Koral, E. Allahyari, S. Amoruso, and A. Andreone, Opt. Laser Technol. **128**, 106159 (2020).
11. A. P. Hibbins, M. J. Lockyear, I. R. Hooper, and J. R. Sambles, Phys. Rev. Lett. **96**, 073904 (2006).
12. J. B. Pendry, L. Martin-Moreno, and F. J. Garcia-Vidal, Science **305**, 847 (2004).
13. L. Martín-Moreno, F. J. García-Vidal, H. J. Lezec, K. M. Pellerin, T. Thio, J. B. Pendry, and T. W. Ebbesen, Phys. Rev. Lett. **86**, 1114 (2001).
14. G. P. Papari, C. Koral, and A. Andreone, Sci. Rep. **9**, 924 (2019).
15. M. N. Gadalla, K. Chaudhary, C. M. Zgrabik, F. Capasso, and E. L. Hu, Opt. Express **28**, 14536 (2020).
16. Y. Zhang, X. Yuehong, C. Tian, X. Quan, X. Zhang, L. Yanfeng, X. Zhang, J. Han, and W. Zhang, Photonics Res. **6**, 18 (2018).
17. P. Li, I. Dolado, F. J. Alfaro-Mozaz, A. Y. Nikitin, F. Casanova, L. E. Hueso, S. Vélez, and R. Hillenbrand, Nano Lett. **17**, 228 (2017).
18. K. Wang and D. M. Mittleman, Phys. Rev. Lett. **96**, 157401 (2006).
19. A. I. Yakimov, V. V. Kirienko, V. A. Armbrister, A. A. Bloshkin, and A. V. Dvurechenskii, Appl. Phys. Lett. **112**, 171107 (2018).
20. H. F. Ghaemi, T. Thio, D. E. Grupp, T. W. Ebbesen, and H. J. Lezec, Phys. Rev. B **58**, 6779 (1998).
21. T. W. Ebbesen, H. J. Lezec, H. F. Ghaemi, T. Thio, and P. A. Wolff, Nature **391**, 667 (1998).
22. S. Fan and J. Joannopoulos, Phys. Rev. B **65**, 235112 (2002).
23. D. R. Smith, D. C. Vier, T. Koschny, and C. M. Soukoulis, Phys. Rev. E **71**, 036617 (2005).